

# Activity and active sites of nitrogen-doped carbon nanotubes for oxygen reduction reaction

Altansukh Dorjgotov · Jinhee Ok · YuKwon Jeon ·  
Seong-Ho Yoon · Yong Gun Shul

Received: 25 September 2012 / Accepted: 27 December 2012 / Published online: 9 January 2013  
© Springer Science+Business Media Dordrecht 2013

**Abstract** Nitrogen-doped carbon (CN<sub>x</sub>) nanotubes were synthesized by thermal decomposition of ferrocene/ethylenediamine mixture at 600–900 °C. The effect of the temperature on the growth and structure of CN<sub>x</sub> nanotubes was studied by transmission electron microscopy, X-ray photoelectron spectroscopy, and Raman spectroscopy. With increasing growth temperature, the total nitrogen content of CN<sub>x</sub> nanotubes was decreased from 8.93 to 6.01 at.%. The N configurations were changed from pyrrolic-N to quaternary-N when increasing the temperature. Examination of the catalytic activities of the nanotubes for oxygen reduction reaction by rotating disk electrode measurements and single-cell tests shows that the onset potential for oxygen reduction in 0.5 M H<sub>2</sub>SO<sub>4</sub> of the most effective catalyst (CN<sub>x</sub> nanotubes synthesized at 900 °C) was 0.83 V versus the normal hydrogen electrode. A current density of 0.07 A cm<sup>-2</sup> at 0.6 V was obtained in an H<sub>2</sub>/O<sub>2</sub> proton-exchange membrane fuel cell at a cathode catalyst loading of 2 mg cm<sup>-2</sup>.

**Keywords** Nitrogen-doped carbon nanotubes · Thermal decomposition · Oxygen reduction reaction · Non-precious metal catalysts

## 1 Introduction

Proton exchange membrane fuel cells (PEMFC) are considered to be a favorable alternative energy source for future energy generations due to their high performance efficiency and low environmental impact. PEMFC have received considerable attention in the recent past because of their high conversion efficiency and low operating temperature (~80 °C), which are favorable for their being used as power sources for portable, automobile, and stationary applications [1]. However, the low operating temperature induces serious problems in the cathode reaction, such as large overpotential for oxygen reduction reaction (ORR). In order to accelerate the rate of oxygen reduction, noble metal catalyst such as platinum is used, which is one of the obstacles hindering the commercialization of PEMFC [2]. Therefore, research and development studies aiming to reduce the amount of platinum catalyst have become increasingly intensive in recent years. There have been many approaches such as improvements in the platinum loading procedures and enhancement of the activity by alloying platinum with low cost metals [2–4]. Besides these attempts, the use of non platinum catalysts such as transition metal macrocycles, chalcogenides, metal carbides, and metal nitrides have been studied extensively [2, 5–7].

Metal–N<sub>4</sub> macrocycles, such as Fe- and Co-macrocycles, are important non-noble catalysts, which have attracted attention due to their reasonable activity and remarkable selectivity toward the ORR. In addition, this class of catalyst usually shows inertness to alcohol oxidation, and many of them can catalyze the ORR to produce water through a four-electron process without significant production of peroxide. A major drawback of the catalyst is its low stability in acidic media (or in the PEMFC operation environment). It has been suggested that this low stability in acidic media can be

A. Dorjgotov · J. Ok · Y. Jeon · Y. G. Shul (✉)  
Department of Chemical and Biomolecular Engineering,  
Yonsei University, Seoul, Korea  
e-mail: shulyg@yonsei.ac.kr

S.-H. Yoon  
Institute for Materials Chemistry and Engineering,  
Kyushu University, Fukuoka, Japan

attributed primarily to the loss of the active site caused by the attack of hydrogen peroxide generated during the oxygen reduction. Heat treatment of the catalysts has been utilized to improve the catalyst stability significantly; in this case, the catalyzed ORR is better suited to a four-electron pathway, producing less hydrogen peroxide. However, this improvement is still insufficient for practical applications [8–10]. These non-noble catalysts have been extensively studied, and the important question of the structure of their active site has been extensively debated [11–15].

Recently, carbon nanotubes (CNTs) have been prepared via pyrolysis of acetonitrile at 900 °C using iron particles supported on alumina as catalyst and have been tested with respect to the ORR [16, 17]. It was proposed that the most probable role of the iron particles is that of a catalyst for both the growth of the CNT and the formation of catalytically more active carbon nanostructures during pyrolysis [16, 17]. However, it was concluded that iron is not part of the active site for the ORR [18]. Several other publications suggest that the metal acts as a catalytic agent that helps to stabilize the nitrogen groups in the graphene sheets and to form carbon nanostructures with a higher degree of edge plane exposure [18–22]. It was also demonstrated that there is neither a correlation between the activity and the metal phase present in the CN<sub>x</sub> nanotubes nor any evidence for the formation of MN<sub>x</sub> sites. However, the ORR activity did not improve by the edge plane in acidic electrolytes using carbon without nitrogen doping [23, 24]. It is thus probable that the presence of nitrogen enhances the electron-donation ability of the graphene sheets. Therefore, the content and species of nitrogen in the carbon material is presumably an important parameter, and elucidation of nitrogen functional groups is of great interest to understand the main active sites for the ORR.

Nitrogen may exist in various forms in the CN<sub>x</sub> nanotubes, including pyridine-like, pyrrole-like, imine-like, and graphitic nitrogen. The relative amount of each species depends on the synthesis conditions such as temperature, the feed material composition, the nitrogen precursor, and the metal catalysts used for the growth. It is reported that the graphitic-N and pyrrolic-N in CN<sub>x</sub> nanotubes is main active sites for ORR [25].

However, more recent studies suggest that the graphitic nitrogen rather than pyrrolic nitrogen is important for the ORR [14, 26]. It is also reported that a heat treatment induce to the formation of more stable nitrogen functional groups [27, 28]. Stanczyk et al. [28] and Pel et al. [29] showed that pyrrolic structures are transformed into pyridinic structures and vice versa via dynamic surface rearrangements during low temperature treatments. At higher treatment temperatures, both the pyrrolic-N and pyridinic-N structures are transformed into more stable quaternary-N. The reaction pathways of the transformation

of the various nitrogen functional groups are complicated. Given the presence of a large variety of carbon structures and different nitrogen-doping methods, detailed studies on the thermal stability of nitrogen-containing functional groups are still not available.

In the present study, we investigate the amount and species of nitrogen functional groups in CN<sub>x</sub> nanotubes grown directly from ethylenediamine at four different temperatures using Fe as a metal catalyst. The thermal stability of these groups is investigated by high-resolution X-ray photoelectron spectroscopy (XPS), and the catalytic activity of undoped and nitrogen-doped CNTs for the ORR is electrochemically studied with the objective of providing more in-depth insight into the nature of the active sites.

## 2 Experimental

### 2.1 Preparation of N-doped carbon nanotubes

The experimental setup for CN<sub>x</sub> nanotube synthesis is illustrated in Fig. 1. The experimental setup used to synthesize CN<sub>x</sub> nanotubes consists of a two-stage tubular quartz furnace. The first stage is the preheater and the second is the growth oven, similar to that reported by Andrews et al. [30] and elsewhere. The synthesis of CN<sub>x</sub> nanotubes was carried out in a furnace system fitted with a quartz tube reactor (80-mm i.d.) at different temperatures (600–900 °C). The precursor solution was prepared by adding 2.5 g ferrocene to ethylenediamine (100 ml) for each run. Prior to feeding the precursor into the reactor, the quartz reactor chamber was flashed with Ar (800 sccm) for 30 min. When the desired temperature was reached, the precursor was introduced into the quartz reactor by an injector with the help of flowing Ar gas (800 sccm) at a feeding rate of 12 ml h<sup>-1</sup>. Fe particles formed from the decomposition of Fe(C<sub>5</sub>H<sub>5</sub>)<sub>2</sub> in the vapor serve as catalysts. The ferrocene concentration in precursor, velocity of carrier gas, and precursor were similar to that reported by Liu et al. [31]. The reaction was allowed to proceed for 3 h. After the reactor is cooled to room temperature in Ar atmosphere, black deposits is collected.

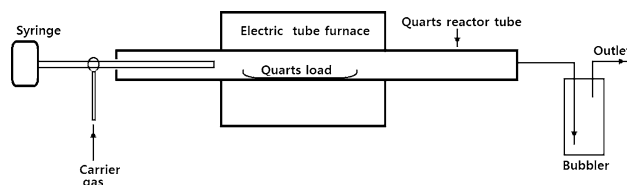


**Fig. 1** Experimental setup for synthesis of CN<sub>x</sub> nanotubes

## 2.2 Physical characterization

Synthesized materials were characterized by transmission electron microscopy (TEM), X-ray photoelectron spectroscopy, Raman spectroscopy, and rotating disk electrode tests, as outlined below.

Raman measurements were performed in the backscattering geometry using a JY LabRam HR instrument fitted with a liquid-nitrogen-cooled CCD detector. The spectra were collected under ambient conditions using the 514.5-nm line of an argon-ion laser. The laser power and the measurement time were 0.5 mW and 90 s, respectively.

The XPS measurements were carried out in an ultra-high vacuum setup equipped with a high-resolution ESCALAB 220i-XL analyzer. A monochromatic Al K $\alpha$  X-ray source (1,486.6 eV; anode operating at 15 kV and 300 W) was used as the incident radiation. The analyzer-slit width was set at 0.3 mm, and the pass energy was fixed at 50 eV for all measurements. The overall energy resolution was better than 1.08 eV. The binding energies were calibrated based on the graphitic C1s peak at 285 eV. The XPS spectra were fitted using the Fityk program with a Gaussian function and Shirley background subtraction. The full width at half maximum (FWHM) values were fixed at a maximum limit of 1.8 eV for all peaks during fitting. TEM images were obtained using a high-resolution Hitachi H-8000 system.

## 2.3 RDE measurements

Rotating disk electrode (RDE) measurements were performed using glassy carbon electrodes ( $\varnothing$  3.1 mm) embedded in Teflon as working electrodes, which were polished on a polishing cloth using alumina powder. The RDE measurements were carried out using an analytical rotator (model RDE80480) and an Autolab potentiostat/galvanostat (PGSTAT30) in a single-compartment glass cell using a three-electrode arrangement. The working electrode was prepared as follows: 10 mg of CN $x$  nanotube was dispersed in mixture of 1 ml ethanol and 80  $\mu$ l 5 % Nafion solution. The suspension was sonicated and stirred for 30 min. Then, 2  $\mu$ l of this suspension was dropped onto the glassy carbon electrode, and the electrode was dried at room temperature. A platinum grid was used as the counter electrode, and a double junction Ag/AgCl/3 M KCl electrode served as the reference electrode. RDE experiments were carried out at a scan rate of 5 mV s $^{-1}$  in the potential range of +0.8 to −0.2 V in 0.5 M H $_2$ SO $_4$ . The electrolyte solution was saturated with oxygen. Commercial Pt/C catalysts (Platinum, nominally 20 wt% on carbon black, Alfa Aesar) and undoped CNT were used for comparison.

## 2.4 Performance tests of membrane-electrode assemblies (MEAs)

The cathode catalyst ink was prepared by ultrasonically blending the catalyst with a Nafion solution (5 wt%, Alfa Aesar) and isopropyl alcohol for 30 min. The catalyst ink was sprayed onto a gas diffusion layer (GDL) (GDL-10bc) until the desired catalyst loading of 2 mg cm $^{-2}$  was achieved. The weight percentages of catalyst and Nafion in the dried cathode layer were 50 and 50 wt%, respectively. The anode catalyst was 40 wt% Pt/C, and the Pt loading was 0.5 mg cm $^{-2}$ . The MEA were hot pressed using a Nafion 212 membrane at 120 °C and 1 atm. for 3 min. The geometric area of the MEA was 1 cm $^2$ . The MEA test was carried out in a single cell. Pure H $_2$  humidified at 75 °C and pure O $_2$  humidified at 75 °C were supplied to the anode and the cathode, respectively. The flow rates of H $_2$  and O $_2$  were 300 and 150 ml min $^{-1}$ , respectively. Polarization experiments were conducted at 75 °C using a fully automated test station without back pressure.

## 3 Results and discussion

Raman spectra of the CN $x$  nanotubes grown at various temperatures are shown in Fig. 2. The D band at  $\sim$ 1,350 cm $^{-1}$  is disorder induced and is associated with optical phonons close to the K point of the Brillouin zone in graphite and carbon nanotubes. The G mode at  $\sim$ 1,585 cm $^{-1}$  is generally regarded as a Raman-allowed  $\Gamma$ -point vibration corresponding to the optical phonon modes of E $_{2g}$  symmetry in graphite, and it is often referred to as the tangential mode for carbon nanotubes. The intensity of the D mode is typically normalized with respect to the intensity of the G mode ( $I_D/I_G$  ratio) for estimating the defect concentration [21, 32]. An increase in the  $I_D/I_G$  ratio with decreasing growth temperature is observed as shown in Fig. 2. Moreover, as the growth temperature increases from 600 to 900 °C, the G-band shifts from 1,596 to 1,574 cm $^{-1}$ , while the D band shifts from 1,358 to 1,344 cm $^{-1}$ . These observations indicate that the G band of the CN $x$  nanotubes shifts to higher wavenumbers with respect to that of multi-walled nanotubes (MWNTs) and that the extent of the shift is correlated to the density of nanobells, and consequently, to the percentage of N in the samples or the concentration of defects.

Figure 3 shows the polarization curves for oxygen reduction on all CN $x$  nanotubes in O $_2$ -saturated 0.5 M H $_2$ SO $_4$  at room temperature using a potential scan rate of 5 mV/s and a rotation rate of 1,600 rpm.

The onset potential for ORR of CN $x$  nanotubes was 0.83 V. As shown in Fig. 3, the ORR activity increases with increasing CN $x$  growth temperature from 600 to

**Fig. 2** Raman spectra of CN<sub>x</sub> nanotubes growth at various temperatures

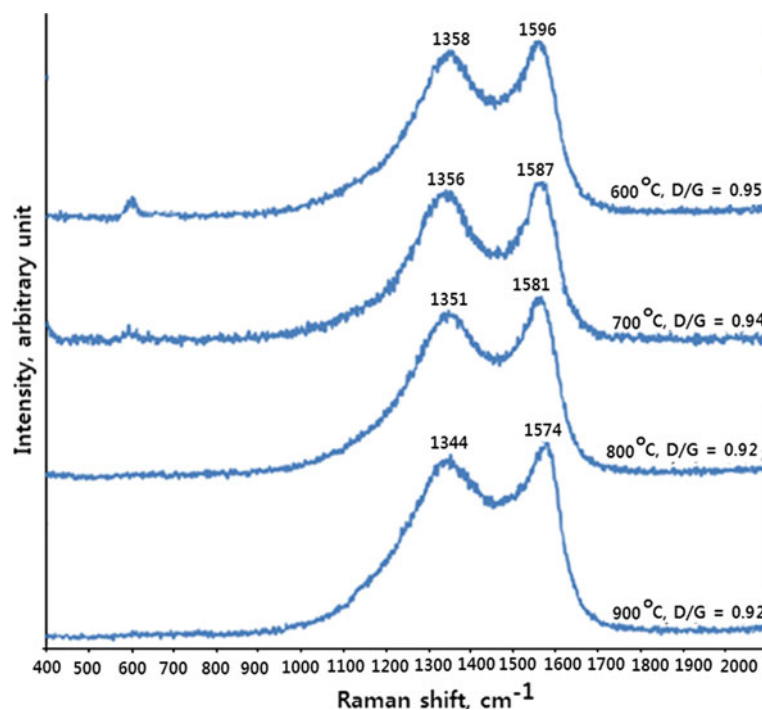
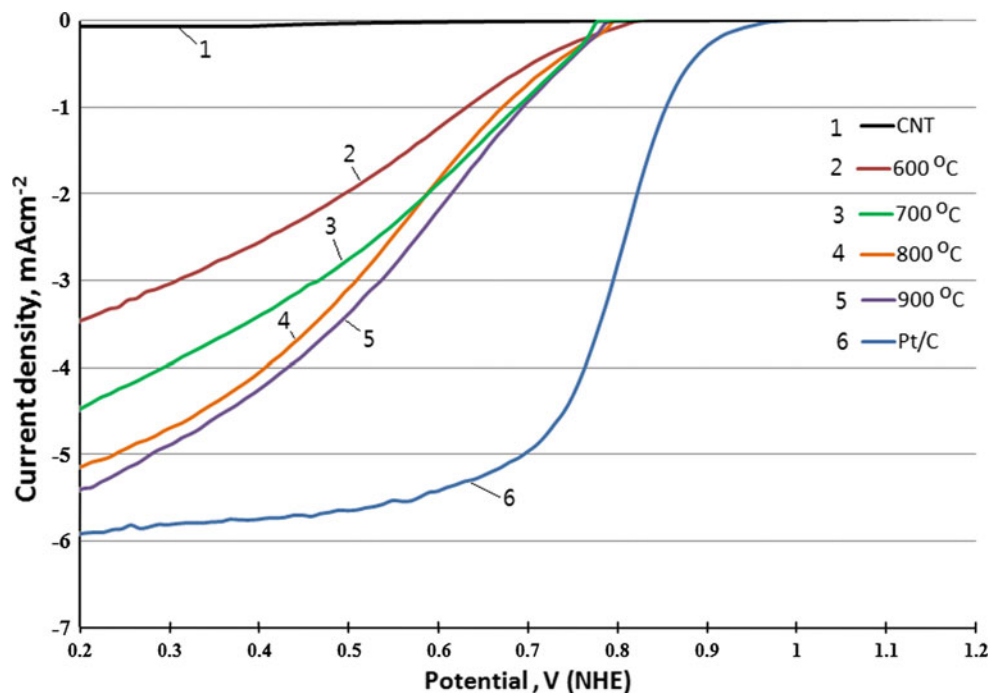


**Fig. 3** Polarization curves of CN<sub>x</sub> nanotubes grown at different temperatures for ORR in 0.5 M H<sub>2</sub>SO<sub>4</sub>; scan rate: 10 mVs<sup>-1</sup> and rotation rate: 1,600 rpm



900 °C. CN<sub>x</sub> nanotubes grown at the synthesis temperature of 900 °C exhibit the best activity among the evaluated nanotubes. However, no clear activity for oxygen reduction is observed in the undoped CNT.

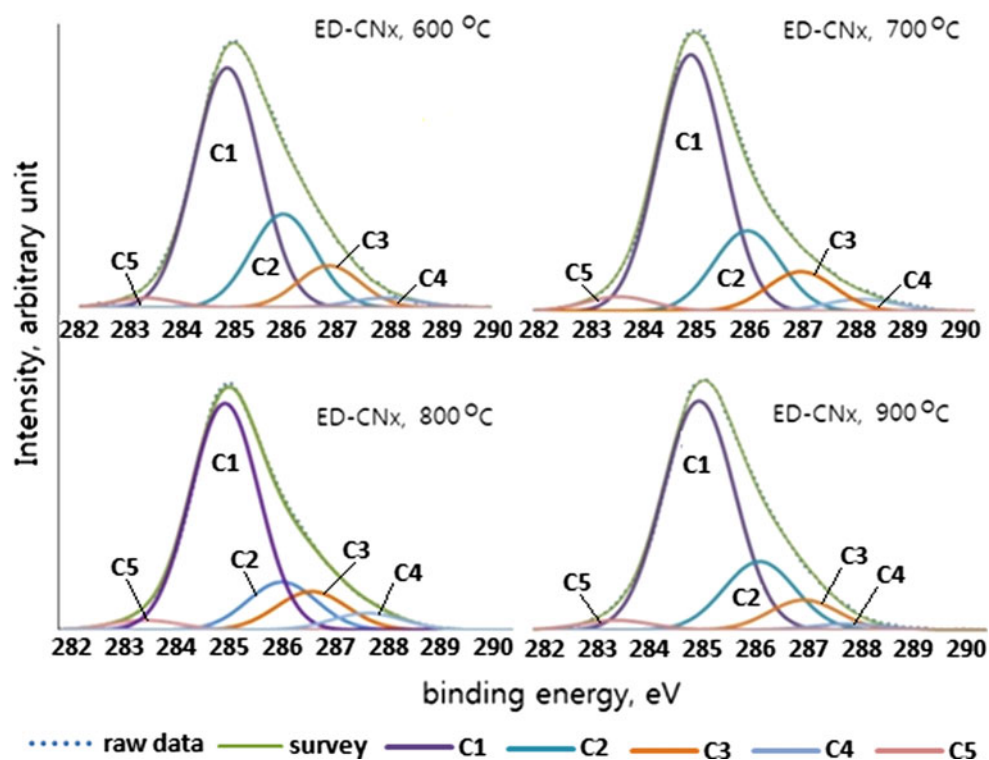
The characterization of the surface nitrogen, carbon, iron, and oxygen of the CN<sub>x</sub> nanotubes by XPS analysis is shown in Table 1 and Figs. 4, 5, 6, 7.

Increasing the synthesis temperature from 600 to 900 °C produces a corresponding decrease in the total nitrogen content of the CN<sub>x</sub> nanotubes from 8.93 to 6.01 at.%, and a decrease in the amount of oxygen from 6.22 to 4.57 at.%. The iron content was independent of the temperature.

The C1s XPS spectra ranging from 282 to 290 eV for CN<sub>x</sub> nanotubes are shown in Fig. 4. In general, there are

**Table 1** Surface elemental concentration of CN<sub>x</sub> nanotubes and relative composition of functional groups

Elemental surface concentration, in atom %	Temperature			
	600 °C	700 °C	800 °C	900 °C
C concentration	82.31	85.20	85.89	87.10
N concentration	8.93	7.30	6.52	6.01
Fe concentration	2.54	2.53	2.65	2.32
O concentration	6.22	4.97	4.94	4.57
Relative composition of nitrogen groups, in atom %				
Fe–N	0.13	0.18	0.19	0.17
Quaternary	1.64	1.65	1.77	2.34
Pyrrolic	5.01	3.02	2.30	1.14
Pyridinic	1.91	2.23	2.07	2.14
Pyridinic oxide	0.24	0.22	0.19	0.22
Relative composition of C groups, in atom %				
Fe–C (C5, 283.4 eV)	1.97	3.05	3.46	3.54
Undamaged alternant hydrocarbon structure (C1, 284.6 eV)	49.91	53.85	57.86	59.62
Damaged alternant hydrocarbon structure (C2, 285.5 eV)	19.12	17.08	12.22	14.21
Free radical defects (C3, 286.3 eV)	8.18	8.40	8.02	8.26
$\pi^* \leftarrow \pi$ shakeup satellite (C4, 287.1 eV)	2.13	2.81	4.35	1.46
Relative composition of O groups, in atom %				
Fe–O (530.28 eV)	0.86	0.6	0.18	0.14
C–O (531.5 eV)	1.69	1.29	1.10	1.54
C=O (532.6 eV)	1.73	1.80	1.75	1.32
O–C=O (533.8 eV)	1.94	1.28	1.91	1.57

**Fig. 4** XPS C1s spectra of CN<sub>x</sub> nanotubes



several types of C groups in the synthesized nanotubes, characterized by the appearance of several spectral peaks: C–Fe at 283.4 eV (C5), C–C at 284.6 eV (C1), C–O at 285.5 eV (C2), C=O and C–N at 286.3 eV (C3), and C–C=O at 287.1 eV (C4) [33].

The peak intensities of the C–C (C1) and C–Fe (C5) species show an increase depending on the growth temperature (Fig. 4; Table 1). The intensity of the carbide peak

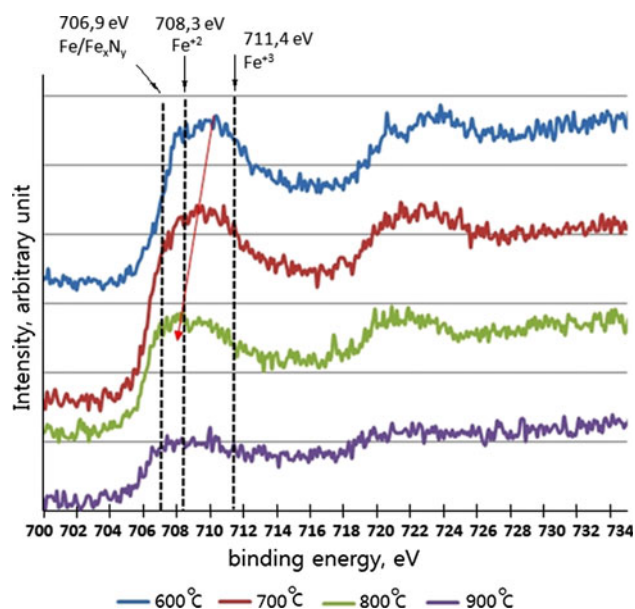
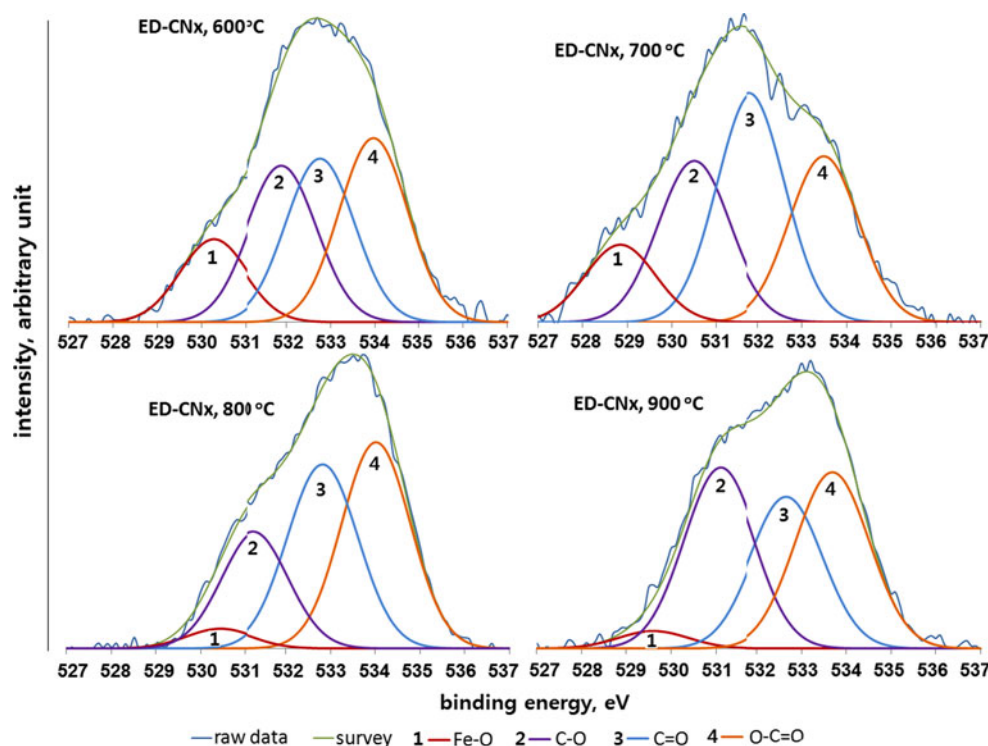


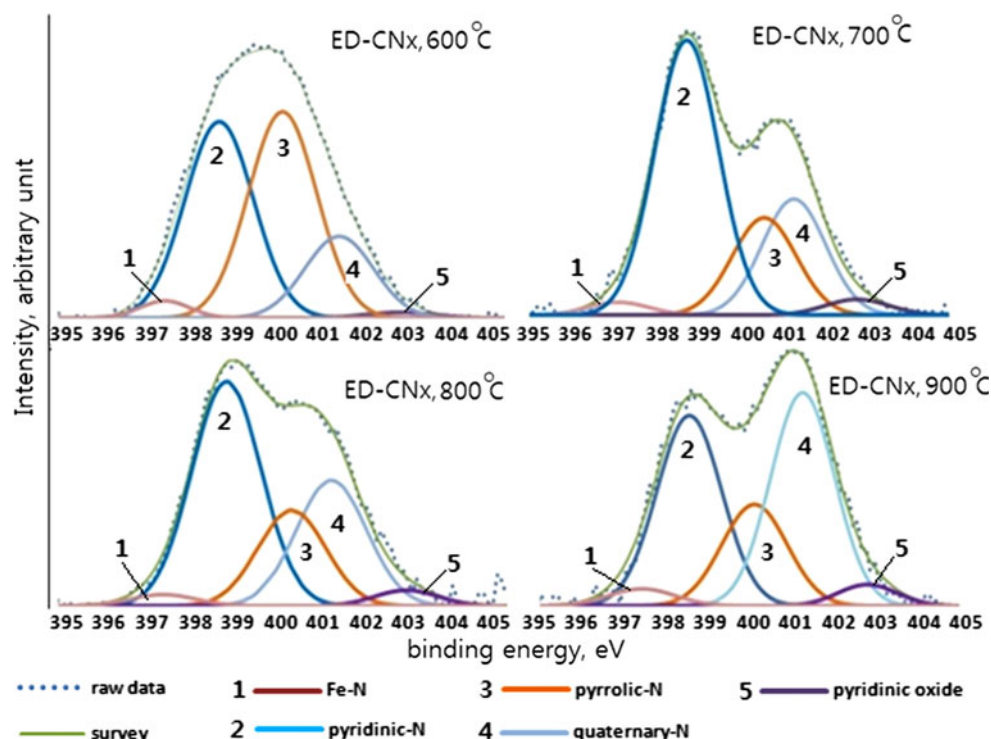
Fig. 5 XPS Fe2p spectra of CN<sub>x</sub> nanotubes

Fig. 6 XPS O1s spectra of CN<sub>x</sub> nanotubes



(C5) at low growth temperatures is observed to be lower than that at high growth temperature. The peak intensity of the CO<sub>x</sub> species (C2–C4) is observed herein to be independent of the temperature. According to a previous report [33], there was no obvious change in the C1s XPS spectra for the non-precious oxygen-reduction catalysts before and after the ORR process. Our data and the data from other reports indicate that the oxygen-containing surface carbon groups (CO<sub>x</sub> species) in the catalysts are not active sites for ORR because the ORR activity was increased with temperature, whereas CO<sub>x</sub> species is independent of the temperature.

Figure 5 shows the Fe2p XPS spectra of the synthesized CN<sub>x</sub> nanotubes. It is observed herein that Fe particles contained in the CN<sub>x</sub> nanotubes are coated with a 1–2.5-nm thick monolayer of graphitic carbon (Fig. 9). It is proposed that the gasified carbon-containing materials may deposit on the Fe particles to produce carbon-coated Fe structures, such as iron/iron carbide, which is a possible active site for ORR and/or may serve as a protective layer to prevent dissolution and oxidation of iron particles in acidic (or PEMFC) conditions. In response to the question of why Fe was detected by XPS, as shown in Fig. 5, there are certain large Fe particles on the surface of the CN<sub>x</sub> nanotubes. These Fe particles are coated by a few atomic layers of carbon; however, the carbon layer thickness is not sufficient to prevent their detection by XPS. The peaks located at 706.9 and 719.9 eV are attributed to

**Fig. 7** XPS N1s spectra of CN<sub>x</sub> nanotubes

metallic Fe and Fe–N, respectively. The peaks appearing at 708.3, 711.4, and 723 eV are indicative of Fe<sup>+2</sup> and Fe<sup>+3</sup>.

The O1s XPS spectra of the nanotubes grown at various temperatures, presented in Fig. 6, were fitted with four components: the peak at 530.28 eV is indicative of a metal oxide, and the other three components are indicative of oxidized carbon species (CO<sub>x</sub>). The peak intensity of the metal oxide is observed to be strongly affected by temperature. At a high temperature, most of the iron species are not oxidized, and they remain as active metal particles due to carbon coating and/or formation of FeN<sub>x</sub> macrocycles (Fig. 6). Evident differences are also present in the Fe2p XPS spectra of the CN<sub>x</sub> nanotubes grown at the various temperatures (Fig. 5). It is also observed that the maximum of the Fe2p<sub>1/2</sub> peak shifts slightly from 710 to 707.5 eV with increasing growth temperature, which indicates that metallic Fe in the sample synthesized at high temperature is less oxidative/more stable than that of lower-temperature samples. At high temperature, big Fe particles (>20 nm) may interact strongly with surrounding atoms such as carbon and nitrogen to generate active macrocycles. It is postulated herein that the encapsulated Fe species in the carbon substrate may exert some electronic effect on the nitrogen-modified active sites and facilitate the ORR. The high temperature heat treatment can also modify the carbon matrix and active sites and enhance the catalytic activity.

An extensive overview of known and possible nitrogen functionalities present in coals and chars was given by Pel

et al. [29]. This report concluded that the nitrogen present in coals and chars is in the form of pyridinic-N (398.6 ± 0.3 eV), pyrrolic-N (400.5 ± 0.3 eV), quaternary-N (401.3 ± 0.3 eV), and pyridinic oxide-N<sup>+</sup>–O<sup>–</sup> (402–405 eV). Further, the iron nitride peak in the N (1s) region is located at 397.4 eV [34].

The N1s XPS of the CN<sub>x</sub> nanotubes is deconvoluted into five peaks (Fe–N, pyridinic-N, quaternary-N, pyrrolic-N and pyridinic-N<sup>+</sup>–O). The detailed deconvolution results are presented in Table 1 and Fig. 7. The total nitrogen content in the CN<sub>x</sub> nanotubes decreases from 8.93 to 6.01 at.%, as the growth temperature is increased. Decrease in the peak intensity of the pyrrolic-N with increasing growth temperature is also detected. In contrast, the amount of quaternary-N is increased with increasing growth temperature. The peak intensity of pyridinic-N was relatively stable with temperature. The peak intensity of Fe–N increases slightly up to the growth temperature of 800 °C and decreases at 900 °C (Table 1; Fig. 7). According to previous studies, the metal-N<sub>4</sub>/N<sub>2</sub> structure is rather decomposed after heat treatment at temperatures of 800 °C or above [18].

The most notable point is that the total nitrogen content, the amount of pyrrolic-N and Fe–O decrease with increasing synthesis temperature, whereas the amount of quaternary-N, nitrogen-containing carbon-coated iron (Fe–C), Fe–N, and the ORR activity increase. Pyridinic-N was relatively stable with temperature. The results of the physical and electrochemical characterizations suggest that

the various nitrogen configurations are not all active sites for ORR, though quaternary-N, Fe–N, and Fe–C (Fe–C–N) may be active sites, meaning that the ORR activity is directly related to the content of quaternary-N, Fe–N, and Fe–C (Fe–C–N), which depends on the synthesis temperature as shown in Fig. 8. However, the pyrrolic-N is inactive species for ORR, because the relationship between amount of pyrrolic-N and ORR activity was inverse.

Many electrocatalytic reactions show increased kinetics on carbon edge planes compared with basal planes. This increase in activity is attributed to the higher tendency of edge planes to chemisorb oxygen [35]. Moreover, pyridinic-N has a lone electron pair in the plane of the carbon matrix, the electron-donating ability of the nitrogen-containing carbon catalyst is increased by this electron pair, thus promoting the electrocatalysis of the oxygen reduction reaction. Liang et al. [32] proposed that the pyridinic-N may be not the definitive ORR active sites; but, according to their research results, the more catalytically active samples contain a higher percentage of pyridinic-N.

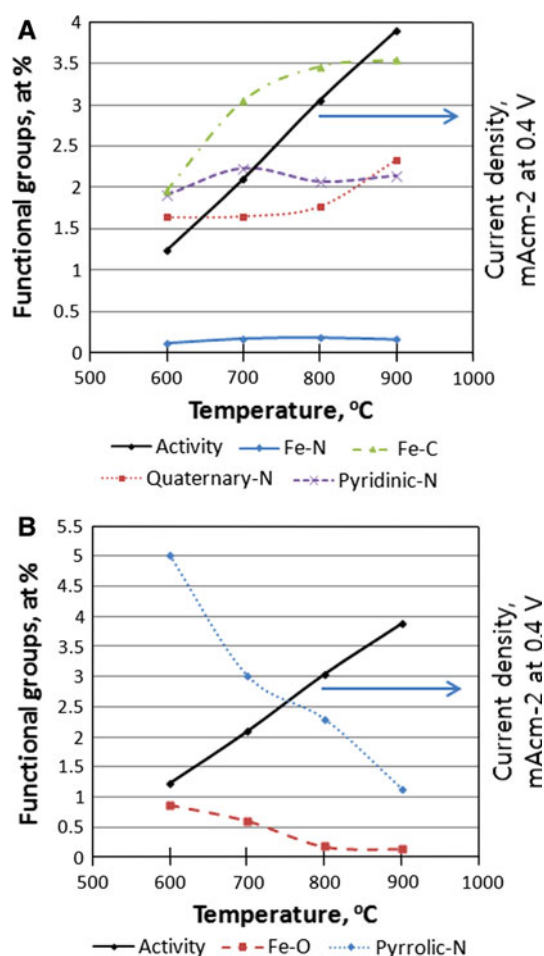


**Fig. 8** Relationship between activity, active or inactive species, and synthesis temperature

It should be mentioned that pyridinic-N contributes one p-electron to the aromatic  $\pi$ -system and has a lone electron pair in the plane of the carbon matrix. The pyridinic-N can be found on the edge of a carbon plane and a carbon vacancy. Thus, it will weaken the O–O bond via the bonding between oxygen and nitrogen and/or the adjacent carbon atom, and facilitate the reduction of oxygen. Ikeda et al. [36] used the Car-Parrinello MD approach to model oxygen reduction on N-doped carbon layers and found that the  $O_2$  molecule is preferentially adsorbed associatively at C sites on graphene-like zigzag edges, if a quaternary-N is located nearby. The subsequent oxygen reduction proceeds mainly by the four-electron reaction pathway with a low free-energy barrier. Quaternary-N bonds to three carbon atoms in the plane of the carbon matrix. These two types of nitrogen are the most stable species present in carbon when heated to 800 °C or higher temperatures [20].

There are two major viewpoints on the nature of the ORR active sites of these nitrogen-modified carbon-based catalysts. First, Fe–N<sub>4</sub> and Fe–N<sub>2</sub> centers bound to the carbon support are believed to be catalytically active and the central transition metal plays a crucial role in the ORR [8–22]. Second, nitrogen functional groups doped in the carbon matrix are believed to be active for the ORR. The transition metals do not take part in the ORR, but the addition of transition metal in the catalyst synthesis facilitates the incorporation of nitrogen into the carbon matrix, which can increase the ORR active site density on the catalysts [25–29].

Based on our research, we support the second opinion on the ORR active sites (more exactly, pyridinic-N, quaternary-N, and nitrogen-containing carbon-coated Fe–C–N).

The Fe–N-type nitrogen constitutes only a very small portion (1.31–2.82 at.%) of the total surface nitrogen species, and the majority of N species is attributed to the other N species, namely pyridinic-N, quaternary-N, pyridinic-N<sup>+</sup>–O, and pyrrolic-N. As shown in Fig. 9, most of the metal particles are located at the end of the nanotubes, meaning that the numbers of carbon and nitrogen atoms surrounding the metal particle are fewer than the number of atoms along the length of the nanotubes. Thus, the peak intensities of Fe–N in the N1s region are consequently very low and slight increases depending on the growth temperature (Fig. 6; Table 1). It is thus difficult to evaluate the effect of Fe–N in this study.

The morphologies of the carbon products obtained are characterized by TEM and the results are shown in Fig. 9. The formation of bamboo-like structures is attributed to the more energetically favorable formation of a positive curvature during the substitution of nitrogen atoms into the graphitic structure. It is noteworthy that the diameter, wall thickness, and compartment distance of CN<sub>x</sub> nanotubes is strongly dependent on the reaction temperature. In order to obtain the diameters and diameter distributions



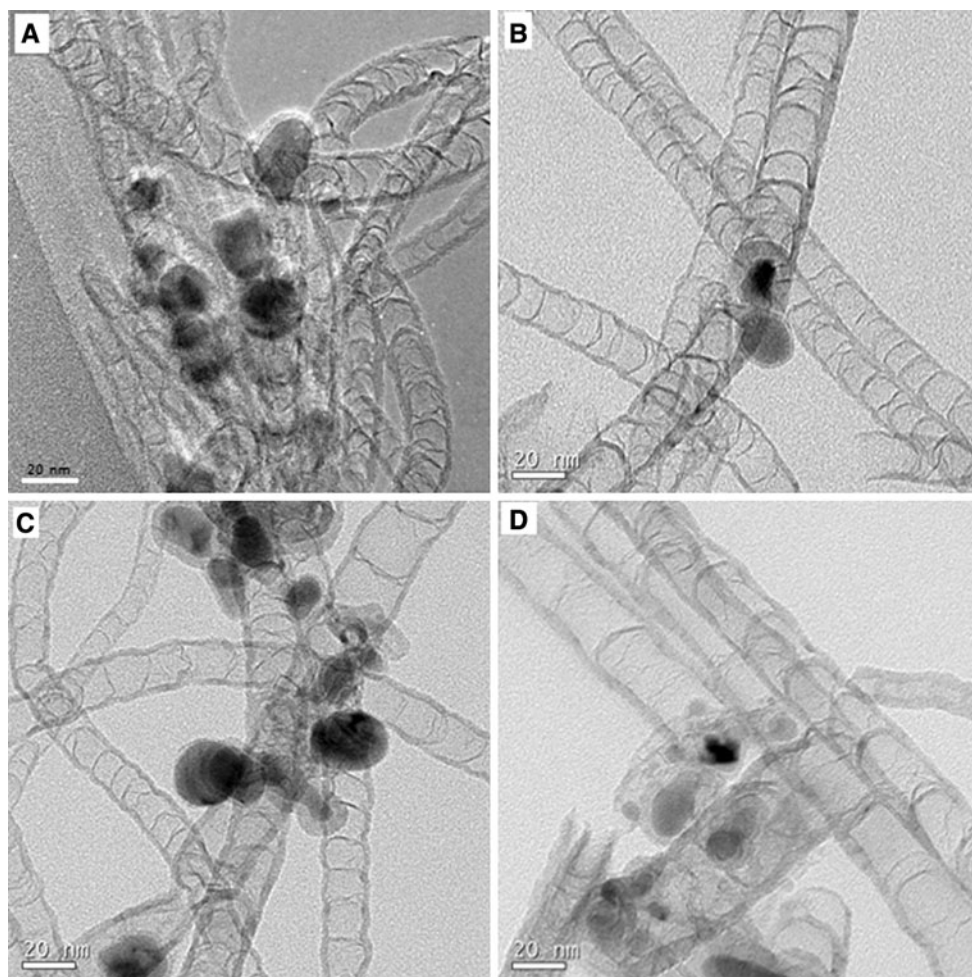


**Fig. 9** TEM images of CN<sub>x</sub> nanotubes **a** CN<sub>x</sub> 600 °C, **b** CN<sub>x</sub> 700 °C, **c** CN<sub>x</sub> 800 °C, **d** CN<sub>x</sub> 900 °C

of CN<sub>x</sub> nanotubes, we have selected more than 100 CN<sub>x</sub> nanotubes per sample and measured their outer diameters from their respective TEM images. It can be seen that the CNTs grown at low reaction temperature have smaller diameter and narrower diameter distribution. With the increase of reaction temperature, the produced CN<sub>x</sub> nanotubes show larger diameter and wider diameter distribution. The average diameters of CN<sub>x</sub> nanotubes grown at 600, 700, 800, and 900 °C were 18, 18.8, 20, and 25 nm, respectively. We believe that the difference in the average diameters of CNTs grown at different temperatures is principally attributed to the agglomeration of metallic iron. At higher reaction temperatures, larger and non-uniform metallic clusters are formed. The compartment distance of CN<sub>x</sub> nanotubes grown at 600, 700, 800, and 900 °C were 12, 13.8, 20, and 31 nm, respectively. The temperature influence on the structure of the carbon materials has been emphasized. It is generally accepted that carbon materials are formed by carbon atom dissolving, diffusing, and precipitating through the catalyst droplets in CVD process [37, 38].

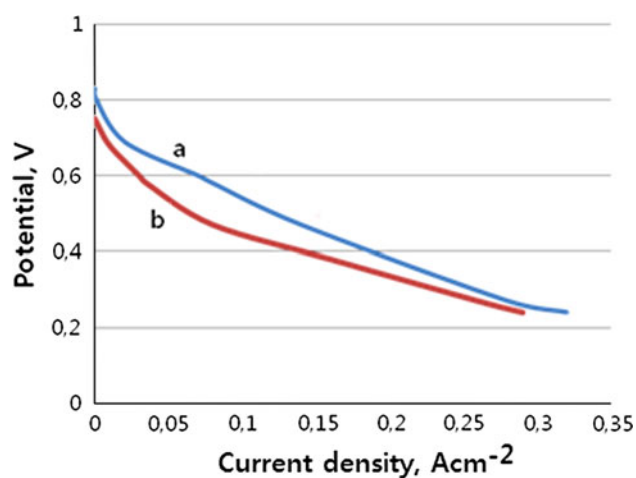


**Fig. 10** Polarization curves of PEM fuel cells fabricated with various cathode catalysts **a** CN<sub>x</sub> at 900 °C and **b** CN<sub>x</sub> at 800 °C

Figure 10 shows the polarization curves of PEM fuel cells fabricated using the CN<sub>x</sub> nanotubes grown at 800 and 900 °C as cathode catalysts. The cathode catalyst loadings

are maintained at  $2 \text{ mg cm}^{-2}$ . The experiments are performed without back pressure on both the anode and cathode compartments. Ohmic potential drop is not compensated in the measurements. The cell performances increase with increasing synthesis temperature, which is indicating an improvement for ORR activity. The open circuit potential and current density of the CN<sub>x</sub>-900 °C catalyst are 0.83 V and  $0.07 \text{ A cm}^{-2}$  at 0.6 V, respectively.

The relationship between the nitrogen species in the N1s region and the loss of catalytic activity is evaluated in a short-term durability test. Figure 11 shows the durability test behavior of PEM fuel cells fabricated using the CN<sub>x</sub> nanotubes grown at 800 and 900 °C as cathode

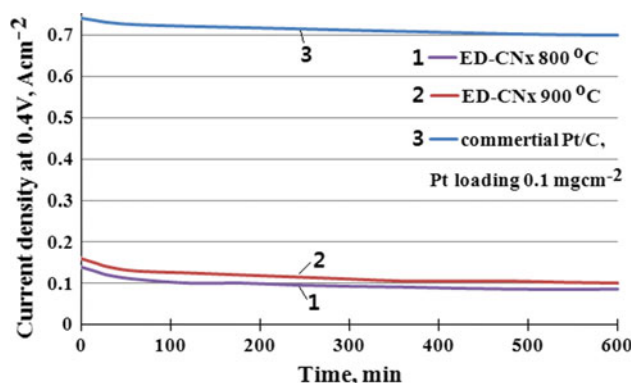


**Fig. 11** Short-term durability test of CN<sub>x</sub> nanotubes used as a catalyst and compared with commercial Pt/C catalyst

catalysts. The cathode catalyst loadings are maintained at  $2 \text{ mg cm}^{-2}$ . Commercial Pt/C catalysts (Platinum, nominally 40 wt% on carbon black, Alfa Aesar) were used for comparison and the Pt loading was  $0.1 \text{ mg cm}^{-2}$ . The experiments are performed without back pressure on both the anode and cathode compartments. In both case the activity decreases significantly during the first 6 h. The cell performance of the CN<sub>x</sub>-900 °C catalyst is higher than that of the CN<sub>x</sub>-800 °C due to the high amount of quaternary-N and nitrogen-containing carbon-coated iron (Fe–C–N) species. This loss of activity appears to be directly related to the protonation of the pyridinic-N and formation of an inactive site.

Following the deconvolution of the N1s XPS data of CN<sub>x</sub>-900 °C (Fig. 12), it becomes obvious that the intensity of the pyridinic-N peak decrease after the short-term stability test. As previously discussed, pyridinic-N is bonded to two carbon atoms in the carbon plane with a basic lone pair of electrons. Given that the lone pair of electrons is not delocalized into the aromatic  $\pi$ -system, the pyridinic-N can be protonate to pyridinic-N–H (the pyridinium cation) in the acidic environment of PEMFCs. The schematic representation of the protonation reaction is also shown in Fig. 12. However, within the accuracy of the XPS measurements, the pyridinic-N–H cannot distinguish from quaternary-N [14]. The peak at 401.3 eV after the stability test may relate with both of quaternary-N and pyridinic-N–H. The small peak at 398.6 eV may result from the remaining pyridinic-N and/or pyridinic-N derived from pyridine-N-oxide.

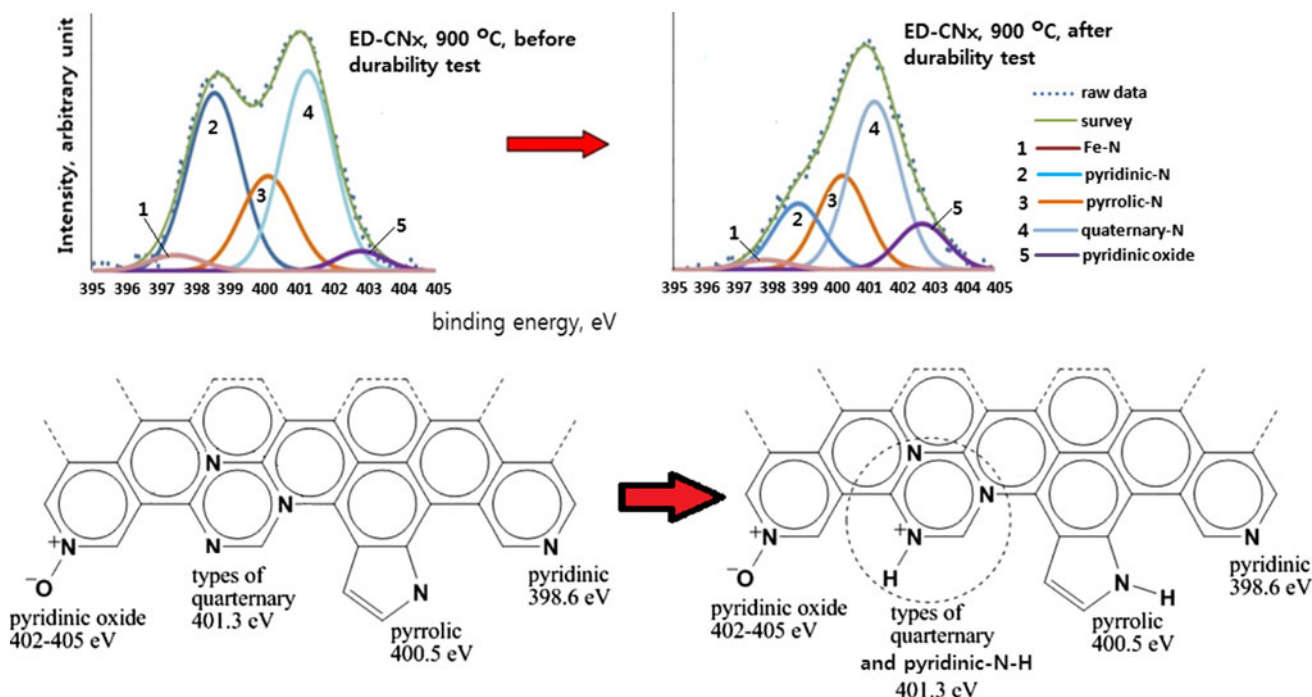


**Fig. 12** N1s XPS data of CN<sub>x</sub> (900 °C) before and after the durability test

The relationship between the N species and the short term durability behavior corroborate the indication that quaternary-N and Fe–C are a stable active sites and pyridinic-N is an unstable active site. In contrast, quaternary-N bond to three carbon atoms in the carbon plane and has not lone pair of electrons, thus less susceptible to protonation. We believe that the loss of activity is indicative of protonation of pyridinic-N and formation of inactive species (pyridinic-N–H). The cell performance was stabilized after 6 h due to stable active sites (quaternary-N, nitrogen-containing carbon-coated iron).

#### 4 Conclusions

In this study, N-doped carbon nanotube is synthesized at various growth temperatures using ethylenediamine as the carbon and nitrogen source and ferrocene as a catalyst. The structure of the CN<sub>x</sub> nanotubes is strongly affected by the growth temperature. The content of total nitrogen and pyrrolic-N is decreased with increasing growth temperature. Pyrrolic-N is unstable at high temperature and may change to other configurations. The amounts of quaternary-N, nitrogen-containing carbon-coated iron (Fe–N and Fe–C) and the ORR activity increase with increasing growth temperature. The ORR activity directly relate to the amount of quaternary-N, Fe–N, and Fe–C species (Fe–C–N), the relative contents of which depend on the growth temperature. The pyrrolic-N may be inactive site for ORR because the relationship between amount of pyrrolic-N and ORR activity was inverse. The results of physical and electrochemical characterizations suggest that all nitrogen configurations are not active species for the ORR, quaternary-N may be stable active sites, and pyridinic-N is an unstable active site for ORR in acidic conditions. The amount of Fe–N in the CN<sub>x</sub> nanotubes is too low, thus it is difficult to evaluate the effect of Fe–N.

**Acknowledgments** This work was supported by a National Research Foundation of Korea Grant (NRF-2009-C1AAA001-2009-00926) funded by the Korean government (Ministry of Education, Science and Technology) and by Economy and Human Resources Development of the Korea Institute of Energy Technology Evaluation and Planning (KETEP) grant (No. 20104010100500) funded by the Korean government (Ministry of Knowledge Economy).

#### References

- O'Hayre RP, Cha SW, Colella WG, Prinz FB (2008) Fuel cell fundamentals, 2nd edn. Wiley, Hoboken
- Wang B (2005) J Power Sources 152:1
- Payne TL, Benjamin TG, Garland NL, Kopasz JP (2008) ECS Trans 16:1081
- Loukrakpam R, Wanjala BN, Yin J, Fang B, Luo J, Shao M, Protsailo L, Kawamura T, Chen Y, Petkov V, Zhong CJ (2011) ACS Catal 1:562
- Lakshmana NR, Kranthi KM, Keerthiga G, Raghuram C (2010) J Appl Electrochem 42:945–951
- Reeve RW, Christensen PA, Dickinson AJ, Hamnett A, Scott K (2000) Electrochim Acta 45:4237
- Zagal JH, Griveau S, Silva JF, Nyokong T, Bedioui F (2010) Coord Chem Rev 254:2755
- Dong G, Huang M, Guan L (2012) Phys Chem Chem Phys 14:2557
- Orellana W (2012) Chem Phys Lett 541:81
- Kruusenberg I, Matisen L, Shah Q, Kannan AM, Tammeveski K (2012) Int J Hydrogen Energy 37:4412
- Bezerra CWB, Zhang L, Lee K, Liu H, Marques ALB, Marques EP, Wang H, Zhang J (2008) Electrochim Acta 53:4937–4951
- Feng Y, Alonso-Vante N (2008) Phys Stat Sol B 245:1792–1806
- Nallathambi V, Lee J-W, Kumaraguru SP, Wu G, Popov BN (2008) J Power Sources 183:34–42
- Liu G, Li X, Ganesan P, Popov BN (2009) Appl Catal B 93:156–165
- Lefèvre M, Dodelet JP, Bertrand P (2000) J Phys Chem B 104:11238–11247
- Kundu S, Nagaiah TC, Xia W, Wang Y, Van Dommele S, Bitter JH, Santa M, Grundmeier G, Bron M, Schuhmann W, Muhler M (2009) J Phys Chem C 113:14302–14310
- Matter PH, Wang E, Arias M, Biddinger EJ, Ozkan US (2007) J Phys Chem C 111:1444–1450
- Yeager E (1984) Electrochim Acta 29:1527–1537
- Matter PH, Wang E, Arias M, Biddinger EJ, Ozkan US (2007) J Mol Catal A 264:73–81
- Matter PH, Wang E, Arias M, Biddinger EJ, Ozkan US (2006) J Phys Chem B 110:18374–18384
- Maldonado S, Morin S, Stevenson KJ (2006) Carbon 44:1429–1437
- Liu J, Webster S, Carroll DL (2005) J Phys Chem B 109:15769–15774
- Strelko VV, Kuts VS, Thrower PA (2000) Carbon 38:1499–1503
- Strelko VV, Kartel NT, Dukhno IN, Kuts VS, Clarkson RB, Odintsov BM (2004) Surf Sci 548:281–290
- Lee K, Zhang L, Lui H, Hui R, Shi Z, Zhang J (2009) Electrochim Acta 54:4704–4711
- Niwa H, Horiba K, Harada Y, Oshima M, Ikeda T, Terakura K, Ozaki J, Miyata S (2009) J Power Sources 187:93–97
- Roy SS, Papakonstantinou P, Okpalugo TIT, Murphy H (2006) J Appl Phys 100:053703–053707
- Stanczyk K, Dziembaj R, Piwowars Z, Witkowski S (1995) Carbon 33:1383–1392
- Pel JR, Kapteijn F, Moulijn JA, Zhu Q, Thomas KM (1995) Carbon 33:1641–1653
- Andrews R, Jacques D, Rao AM, Derbyshire F, Qian D, Fan X, Dickey EC, Chen J (1999) J Chem Phys Lett 303:467–474
- Liu J, Czerw R, Carroll DL (2005) J Mater Res 20:538–543
- Liang EJ, Ding P, Zhang HR, Guo XY, Du ZL (2004) Diam Relat Mater 13:69–73
- Gong K, Chakrabarti S, Dai L (2008) Angew Chem Int Ed 47:5446–5450
- Torres J, Perry CC, Bransfield SJ, Fairbrother DH (2003) J Phys Chem B 107:5558–5567
- Shao Y, Zhang S, Engelhard MH, Li G, Shao G, Wang Y, Liu J, Aksay IA, Lin Y (2010) J Mater Chem 20:7491–7496
- Ikeda T, Boero M, Huang SF, Terakura K, Oshima M, Ozaki J (2008) J Phys Chem C 112:14706–14709
- Muataz AA, Ahmadun F, Guan C, Mahdi E, Rinaldi A (2006) NANO 01:251–257
- Chen L, Liu H, Yang K, Wang J, Wang X (2008) J Mater Chem Phys 112:407–411